

# Search for galactic axions with a traveling wave parametric amplifier

QUAX<sup>1</sup>

<sup>1</sup>*INFN*

(Dated: March 8, 2023)

A traveling wave parametric amplifier has been integrated in the haloscope of the QUAX experiment. A search for dark matter axions has been performed with a high Q dielectric cavity immersed in a 8 T magnetic field and read by a detection chain having a system noise temperature of about 2.1 K at the frequency of 10.353 GHz. Scanning has been conducted by varying the cavity frequency using sapphire rods immersed into the cavity. For the eight scans the sensitivity of the instrument was at the level of viable axion models.

## I. INTRODUCTION

The axion is an hypothetical particle that arises from the spontaneous breaking of the Peccei-Quinn symmetry of QCD, introduced to solve the so called strong CP problem [1–3]. It is a pseudoscalar neutral particle having negligible interaction with the ordinary matter, making it a favourable candidate as a main component of dark matter [4]. Cosmology and astrophysical considerations, suggest an axion mass range  $1 \mu\text{eV} < m_a < 10 \text{ meV}$  [5]. The hunt for axion is now world spread and most of the experiments involved in this search use detectors based on the haloscope design proposed by Sikivie [6, 7]. Among them are ADMX [8–11], HAYSTAC [12, 13], ORGAN [14, 15], CAPP-8T [16, 17], CAPP-9T [18], CAPP-PACE [19], CAPP-18T [20], CAST - CAPP [21], GrA-Hal [22], RADES [23–25], TASEH [26], QUAX [27–32], and KFLASH [33, 34]. Dielectric and plasma haloscopes have also been proposed, the most notable examples being MADMAX [35, 36] and ALPHA [37, 38], respectively. The haloscope concept is based on the immersion of a resonant cavity in a strong magnetic field in order to stimulate the inverse Primakoff effect, converting an axion into an observable photon [39]. To maximise the power of the converted axion, the cavity resonance frequency has to be tuned to match the axion mass, while larger cavity quality factors  $Q$  will result in larger signals. Different solutions have been adopted to maximize the signal-to-noise ratio, facing the problem from different angles. Resonant cavities of superconductive and dielectric materials are becoming increasingly popular because of their high  $Q$  [40–43]. In this work we describe the results obtained operating the haloscope of the QUAX- $a\gamma$  experiment, based on an high-Q dielectric cavity immersed in a static magnetic field of 8 T. The cavity is cooled down to  $\sim 100 \text{ mK}$  to allow operation of a traveling wave parametric amplifier operating at about the quantum limit. This is the first operation of a high frequency haloscope (above 10 GHz) with a quantum limited wide band amplifier. A key step in the realization of an apparatus capable of searching for dark matter axions over an extended mass region. Section II describes the experimental set-up with the characterization of all the relevant components, while in Section IV details in the data analysis procedure are given. Since no positive sig-

nals have been detected, in the same Section upper limits for the axion-photon coupling are deduced.

## II. EXPERIMENTAL SETUP

### 1. General description

The core of the haloscope is an extremely high-Q resonant cavity. The cavity is extensively described in [44]: it is based on a right circular copper cavity with hollow sapphire cylinders that confine higher order modes around the cylinder axis. The useful mode is a TM<sub>030</sub>, which has an effective volume  $V \cdot C_{030} = 3.4 \times 10^{-2}$  liters at the resonant frequency of 10.353 GHz, where  $C_{030}$  is a geometrical factor entering in the signal-power estimation in Eq. (9). Under an 8 T-field we measured an internal quality factor of more than  $9 \times 10^6$  at a temperature of about 4 K.

The principle scheme of the measurement set up is shown in Figure 1. The microwave cavity is immersed in a 8 T magnetic field, not shown in the figure, generated by a superconducting solenoid. The microwave cavity is read by a tunable dipole antenna with coupling  $\beta$ . The antenna is the inner core of a superconducting rf cable, for which the final dielectric insulation and metallic shielding have been removed for a length of XX mm. The antenna position is determined by a spring placed between the cavity top and the outside of the rf cable and acting against an electrical motorised linear drive placed at room temperature and connected with a thin steel wire. Precise positioning with an electronic controller is possible over a length of about 20 mm, that allows for  $\beta$  values in the range 1 to 20. Due to tight mechanical constraints, we choose to have the cavity only in the overcoupled regime. A weakly coupled port (coupling about xx) is used for calibration purposes and is connected to the room temperature electronics by means of line L1. To avoid thermal power inputs from room temperature, a 20 dB attenuation is inserted on L1.

Cavity tuning was obtained by displacing triplets of 2 mm-diameter sapphire rods relative to the top and bottom cavity endcaps [44]. Again, independent motion of the two triplets is obtained by mechanical feed-throughs controlled by a room temperature motorised linear posi-

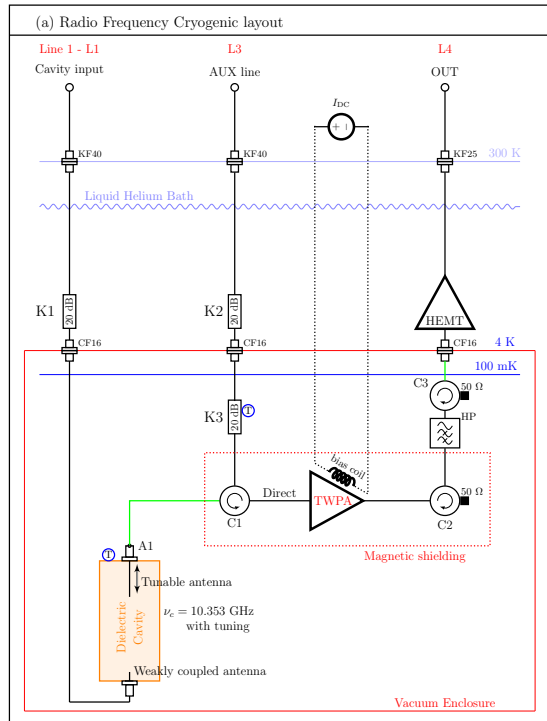


FIG. 1. Schematics of the experimental apparatus. The microwave cavity (orange) is immersed in the uniform magnetic field (not shown) generated by the magnet. C1, C2 and C3 are circulators, HP is a 8 GHz high pass filter, HEMT is a High Electron Mobility Transistors. K1, K2, and K3 are attenuators, shown with their reduction factor in decibels. The components kept in the high vacuum region are enclosed in a red box. Circled T are RuO thermometers. KF40 and KF25 are rf feed-through with ISO-KF 40 and ISO-KF 25 flanges, respectively. CF16 are rf feed-troughs with ConFlat 16 flange. Superconducting NbTi rf cables are in green.

The antenna output is fed onto a circulator (C1) using a superconducting NbTi cable. C1 is directly connected to the input of a traveling wave parametric amplifier (TWPA)[45], which serves as pre-amplifier of the system detection chain. Further amplification at a cryogenic stage is done using a low noise HEMT amplifier (Low Noise Factory model LNA4-16). In order to avoid back action noise from the HEMT, a pair of isolators (C2 and C3) and a 8 GHz High Pass filter are inserted between the TWPA and the HEMT. The output of the cryogenic HEMT is then delivered to the room temperature electronics (RTE) described in figure 2: we refer to this line as L4. The signal line L4 in the RTE features a room temperature HEMT (Low Noise Factory model LNA4-16), whose output is split in two using a power divider (Macom 1147). One output is fed into a spectrum analyser (SA), used for diagnostic and calibration. The input of the SA is referred as measurement point P4. The other output of the splitter is down-converted using a mixer (MITEQ IRM0812LC2Q) driven by the sig-

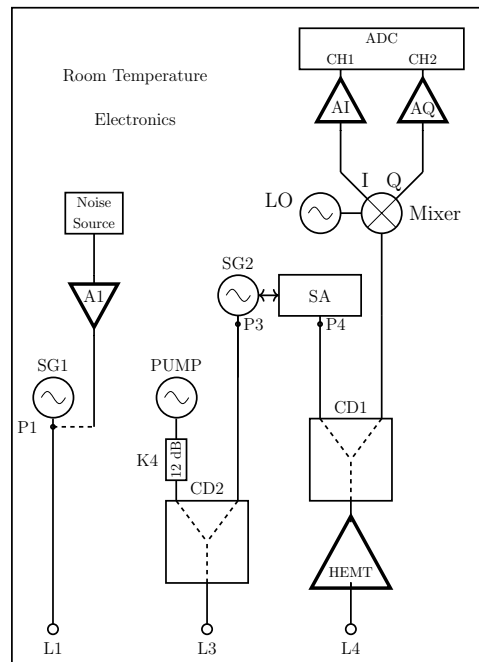


FIG. 2. Room temperature electronics. CD1 and CD2 are power splitters/combiners; LO, SG1, SG2 and PUMP are signal generators; HEMT is a High Electron Mobility Transistor; SA is a spectrum analyser; AI, AQ are low frequency amplifiers; A1 is a rf amplifier; ADC is an analog to digital converter with inputs CH1 and CH2. The signal generator SG2 can be controlled by the spectrum analyser for tracking. The lines L1, L3, and L4 are connected to the corresponding lines in Figure 1.

nal generator LO (Keysight N5183B), set to a frequency about 500 kHz below the cavity resonance. The mixer input level for the local oscillator input has been set to 12 dBm. The room temperature chain is the same used in our previous measurements [28]: the low frequency in phase and quadrature outputs of the mixer are amplified (FEMTO DHPVA-100) and then sampled with a 2 Ms/s analog to digital converter (ADC) and stored on a computer for off line data analysis. Data storage is done with blocks of about 4 s of sampled data for both output channels of the mixer.

The auxiliary line L3 is used for calibrations and to provide the pump signal to the TWP: it is connected to the line L4 by means of the circulator C1, and 20+20 dB of attenuation prevents thermal leakage from room temperature components and from the bath at 4 K.

The room temperature electronic features also a Vector Network Analyser (VNA) for measurement of the scattering parameters S12 (input from line L2 - output from line L1), S31 and S32. From these scattering parameters it is possible to derive the loaded quality factor  $Q_L$ , resonance frequency  $f_c$  and coupling  $\beta$  of the tunable antenna. A diode noise source, having an equivalent noise temperature of about  $10^4$  K, can be fed to line L1 for testing after being amplified in such a way to have an equivalent

noise temperature inside the microwave cavity slightly in excess of the thermodynamic temperature. A microwave signal generator and a microwave spectrum analyser are used for the measurement of the system noise temperature as described below. All rf generators, the VNA and the spectrum analyser are frequency locked to a GPS disciplined reference oscillator.

Finally, a dc current source is connected to a superconducting coil used to bias the TWPA.

Following the figure, all components below the horizontal blue line sectioning the 4K region are enclosed in a vacuum chamber immersed in a liquid helium cryostat. Two Ruthenium Oxide thermometers measures the temperature of the cavity and of attenuator K3, respectively.

## 2. Dilution unit

The cryogenic and vacuum system is composed of a cryostat and a  $^3\text{He}$ - $^4\text{He}$  wet dilution refrigerator. The cryostat is a cylindrical vessel of height 2300 mm, outer diameter 800 mm, inner diameter 500 mm (made by Precision Cryogenics System Inc). The dilution refrigerator is a refurbished unit (made by Leiden Cryogenics Inc.) previously installed in the gravitational wave bar antenna Auriga test facility [46]. Such dilution unit has a base temperature of 70 mK and cooling power of 1 mW at 120 mK. The DU is decoupled from the gas handling system through a large concrete block sitting on the laboratory ground via a Sylomer carpet where the Still pumping line is passing. This assembly minimizes the acoustic vibration induced on the TWPA, which is rigidly connected to the mixing chamber. Once the Helium cryostat has been filled up with liquid helium the DU column undergo a fast pre-cooling down to liquid-helium temperatures via helium gas exchange on the Inner Vacuum Chamber (IVC). This cooling down operation take almost 4 hours. When a temperature of 4 K has been reached, the pre-cooling phase ends, the inner space of the IVC is evacuated. From that point on the dilution refrigerator takes over and the final cooling temperature of around 80 mK is attained after about 5 hours. No charcoal pump was present in the DU cooled system. A pressure of around  $10^{-7}$  mbar was monitored without pumping on the IVC room temperature side through all the experimental run. Temperatures are measured with a set of different thermometers. Most of them are used to monitor the behaviour of the dilution unit.

## 3. Magnet system

A NbTi superconducting solenoid provides the background field of 8 T (value at centre of the magnet), charged at a final current of 92 A with a ramp rate not exceeding 7 mA/s to reduce eddy currents losses in the ultra-cryogenic environment. When the current reaches the nominal value, a superconducting switch can be acti-

vated and the magnet enters in persistent mode. In this mode, the stability assures a loss of the magnetic field lower than 10 ppm/h. For this measurement campaign such mode was actually not used, and the magnet was kept connected to the current source. The magnet has an inner bore of diameter 150 mm, and a length of 450 mm. When the magnet is driven by the 92 A current, the effective squared field over the cavity length amounts to  $50.8 \text{ T}^2$ .

The magnet is not actively shielded, so the TWPA and sensible electronics would be exposed to a stray field in the range of 2-3 kG along his length, well above the operative conditions. In order to reduce the stray field in the area of the TWPA, a counter field is locally generated by an additional superconducting solenoid, made of NbTi superconducting wire (0.8 mm diameter) wound on an Aluminium reel. The inner diameter of this winding is 77.8 mm and its height is 250 mm. The shield winding is biased in series to the main 8 T magnet, so it is able to reduce the field in the volume occupied by the TWPA, at any field strength, to a mean value of 400 Gauss. To shield such remaining field a hybrid box is encapsulating the two circulators C1 and C2 and the TWPA. This hybrid box is constituted by an external box of lead and an internal one of cryoperm. The box dimension is  $35 \times 65 \times 210 \text{ mm}^3$ , with one small base opened to allow cabling, and is thermally anchored to the dilution unit (DU) mixing chamber.

## 4. Amplifier characterization

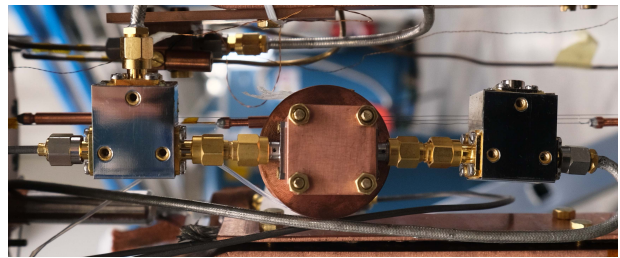


FIG. 3. Picture of the traveling wave parametric amplifier (TWPA). The TWPA is enclosed in the central square box, the circle on the background is the holder of the superconducting coil providing the bias magnetic field. The two 3-port boxes are isolator C2 (on the right) and circulator C1 (on the left).

The TWPA, see Figure 3, has been characterised following the procedure described in Ref. [47]. In particular its working point in term of bias current  $I_b$ , pump frequency  $f_P$  and pump amplitude  $A_p$  has been chosen in order to minimize the system noise temperature  $T_{\text{sys}}$  at the cavity unshifted frequency  $\nu_c$ . The performances of the TWPA have been measured several times with the magnetic field off, and then with the magnet energized once to 4 T and once to 8 T. All the resulting values of  $T_{\text{sys}}$

are compatible, around 2.0 K. During the magnet current ramp up we monitored the wide bandwidth gain of the amplifier, to look for possible variations of the working point induced by stray field passing through the shielding. No changes have been observed, indicating that the stray magnetic field permeating the shields is below a flux quanta for the Josephson junctions of the TWPA. The wide bandwidth gain of the amplifier is shown in Figure 4(a). The pump frequency is set to  $f_P = 9.4181$  GHz, with  $A_p = -16.5$  dBm, and  $I_b = -1.38$  mA. It is evident from the figure that large (10 dB) oscillations of the gain are present in the useful region, i.e. in the 10 - 11 GHz interval. By precisely varying bias and pump frequency it is possible to align a gain maximum to the cavity frequency: a gain maximum is normally equivalent to a minimum system noise temperature. Figure 4(b) shows the gain in a 4 MHz interval centred at the cavity resonant frequency. The two gain profiles are obtained with two different values of pump amplitude: higher gains means a much sharper gain profile, but even for the sharpest one a useful region of flat gain of about 1 MHz is obtained.

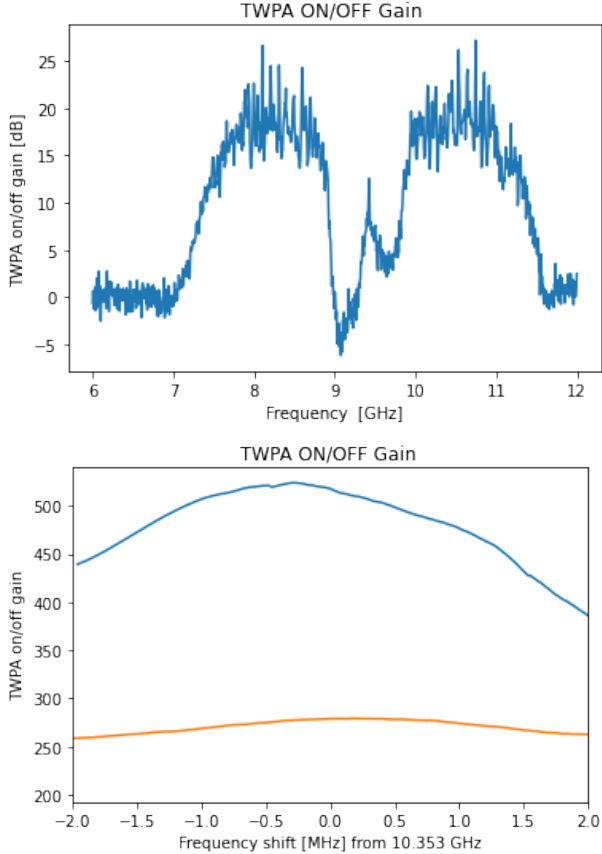


FIG. 4. Wide (a) and small (b) bandwidth gain of the traveling wave parametric amplifier.

Table I shows the measured values of system noise temperatures, all of them measured at the test frequency  $\nu_c = 10.353$  GHz with the pump at  $f_P = 9.4181$  GHz. The table shows cavity and attenuator temper-

n	Magnetic field (T)	Cavity Temp (K)	$T_{\text{sys}}$ (K) On Resonance	K3 Temp (K)	$T_{\text{sys}}$ (K) Off Res
1	0	0.12	$2.12 \pm 0.05$	0.18	$2.22 \pm 0.06$
2	0	0.12	$2.04 \pm 0.03$	0.19	$1.94 \pm 0.03$
3	4.0	0.13	$2.11 \pm 0.03$	0.22	$2.16 \pm 0.03$
4	0	0.12	$1.89 \pm 0.04$	0.18	$1.98 \pm 0.05$
5	8.0	0.11	$2.23 \pm 0.06$	0.18	$2.26 \pm 0.06$

TABLE I. Summary of measurement of system noise temperature  $T_{\text{sys}}$  at the cavity main frequency  $\nu_c \simeq 10.353$  GHz.

ature, which contributes in different ways to the noise: the off cavity resonance value refers to a frequency 1 MHz detuned by  $\nu_c$ , where only the attenuator noise is seen by the TWPA, while on resonance a combination between cavity noise and attenuator noise forms the input noise. Only for the case of critical coupling ( $\beta = 1$ ), the noise at the cavity frequency is determined only by the cavity temperature. Except for the case  $n=5$  (Magnetic field 8 T), having  $\beta = 12$ , the other measurements have  $\beta = XX$ . One extra measurement has been done at the frequency  $\nu_{c,2} = 9.404061$  GHz, where another cavity mode is present. For such measurement the pump frequency was set to  $f_{P,2} = 8$  GHz, for a resulting  $T_{\text{sys}}(\nu_{c,2}) = 2.1 \pm 0.1$  K.

For the main cavity mode, the average value is  $T_{\text{sys}}^{\text{avg}} = 2.06 \pm 0.13$  K on resonance, and  $T_{\text{sys}}^{\text{avg}} = 2.07 \pm 0.14$  K off resonance. The central values come from the weighted average, while their errors are the standard deviation of all the values, showing a much wider distribution compared with the error of the single values. The resulting gain for the detection chain, from point A1 in Figure 1 to point P4 in Figure 2 is  $74.7 \pm 0.1$  dB. We have also obtained the gains for the other two rf lines, resulting in  $-61.3 \pm 0.1$  dB from point P1 to A1, and  $-50.9 \pm 0.1$  dB from point P3 to A1. All these gain values are those in the presence of magnetic field at 8 T.

We can try now to evaluate all the various contributions to the measured noise level. In the quantum regime ( $k_B T \ll h\nu$ ), the number of noise photons at frequency  $\nu$  emitted by a thermal source is given by

$$N(\nu, T) = \frac{1}{2} \coth\left(\frac{h\nu}{2k_B T}\right), \quad (1)$$

where  $h$  is Planck constant,  $k_B$  is Boltzmann constant,  $T$  is a thermodynamic temperature. At the considered temperatures, the noise is entirely due to quantum fluctuations, as the contribution of the thermal photons is negligible.

At a given signal frequency  $\nu_s$ , the noise power spectral density at the output of the HEMT amplifier is

$$\begin{aligned} \text{PSD}_{\text{HEMT}}(\nu_s) = & G_{\text{HEMT}} [N_{\text{HEMT}} + (1 - \Lambda_2) N_2 + \\ & \Lambda_2 G_{\text{TWPA}} (N_{\text{TWPA}} + (1 - \Lambda_1) N_1 + \\ & \Lambda_1 N(\nu_s, T_s) + \Lambda_1 N(\nu_i, T_i))] h\nu_s \end{aligned} \quad (2)$$



where  $G_{\text{TWPA}}$  is the net gain of the TWPA,  $N_{\text{TWPA}}$  and  $N_{\text{HEMT}}$  are the added noise of the TWPA and HEMT, respectively.  $\Lambda_1 < 1$  is the gain of the lossy chain from point A1 to the TWPA and, analogously,  $\Lambda_2 < 1$  is the gain from the output of the TWPA to the HEMT;  $N_1$  and  $N_2$  are the noise contributions coming from a simple beam splitter model for a lossy element.

$N(\nu_s, T_s)$  and  $N(\nu_i, T_i)$  represent the quantum noise contributions at the signal frequency equal to the cavity frequency,  $\nu_s = \nu_c$ , and at the idler frequency,  $\nu_i = 2f_P - \nu_c$ , respectively. At the idler frequency the noise source is the attenuator K3, whose temperature is measured by one of the two thermometers. Its temperature has actually to be increased by the power leakage coming from the 4 K stages, attenuated about a factor 100 exactly by K3, i.e. we added 40 mK to the thermodynamic temperature of K3. At the signal frequency, the effective temperature is an intermediate value between the cavity temperature and the temperature of K3, the exact value depending on the coupling  $\beta$ : for  $\beta = 1$  we have just the cavity temperature.

The line gains are estimated at room temperature for the non-superconducting cabling, resulting in  $\Lambda_1 \simeq -0.3$  dB and  $\Lambda_2 \simeq -0.7$  dB, giving in linear units values very close to 1. Such gains show low losses for the lines and allowed us to neglect the noise contributions  $N_1$  and  $N_2$  in Equation (2). In addition, the high gain of the HEMT allows us to neglect all the noise contribution entering after its amplification.

With such simplifications, Eq. (2) can be recast to estimate the total system noise (referred at the point A1),

$$\text{PSD}_{\text{A1}}(\nu_s) = \frac{\text{PSD}_{\text{HEMT}}(\nu_s)}{\Lambda_1 \Lambda_2 G_{\text{TWPA}} G_{\text{HEMT}}} = N_{\text{sys}} h \nu_s, \quad (3)$$

where we have defined  $N_{\text{sys}}$  as the total number of noise photons for the system, obtaining

$$N_{\text{sys}} \simeq N(\nu_s, T_s) + N(\nu_i, T_i) + \frac{N_{\text{TWPA}}}{\Lambda_1} + \frac{N_{\text{HEMT}}}{\Lambda_1 \Lambda_2 G_{\text{TWPA}}}. \quad (4)$$

Giving the measured value  $T_{\text{sys}} = 2.06 \pm 0.13$  K, we obtain in terms of photons a noise level:

$$N_{\text{sys}} = \frac{k_B}{h \nu_s} T_{\text{sys}} = 4.2 \pm 0.3. \quad (5)$$

In order to disentangle the contribution of the HEMT, we measured the system noise with the TWPA off (without pump and bias). The resulting noise temperature in this case was  $49 \pm 1$  K, with a total gain reduced by a factor 125. The contribution of the HEMT to the total noise temperature is then  $0.39 \pm 0.01$  K. Table II summarises the noise contributions and allows to derive the TWPA added noise as  $N_{\text{TWPA}} \simeq 2.1$  photons at the frequency of 10.353 GHz.

Term	Value (K)	$N$ photons
$N(\nu_s, T_s)$	0.27	0.5
$N(\nu_i, T_i)$	0.27	0.7
$N_{\text{HEMT}}/\Lambda_1 \Lambda_2 G_{\text{TWPA}}$	0.39	0.8
$N_{\text{sys}}$	2.06	4.2
$N_{\text{TWPA}}/\Lambda_1$		2.2

TABLE II. Noise contributions to the system noise. The following values have been used:  $\nu_s = 10.353$  GHz,  $\nu_i = 7.94$  GHz,  $T_s = 0.16$  K,  $T_i = 0.22$  K.  $N_{\text{TWPA}}/\Lambda_1$  is the difference between the measured  $N_{\text{sys}}$  and the sum of the preceding terms.

RUN n	$\nu_c$ (GHz)	Duration (s)	$T_c$ (mK)	$T_{\text{K3}}$ (mK)
389	10.353 525	2000	113	177
392	10.353 499	2000	111	178
394	10.353 473	2000	112	181
395	10.353 473	4000	113	185
397	10.353 444	2000	114	182
399	10.353 424	4800	112	177
401	10.353 399	28000	110	176
404	10.353 368	2000	110	176

TABLE III. Summary of the RUNs performed for the axion dark matter search. The cavity frequency is the value determined via a fast tracking spectrum on the SA. The frequency of the LO has been set to 10.353 GHz for all RUNs but RUN 404, where it is set to 10.3529 GHz.  $T_c$  and  $T_{\text{K3}}$  are the cavity and attenuator K3 temperatures, respectively.

### 5. Data taking

The search for axion dark matter has been performed over a time span of about 17 consecutive hours. The cavity antenna coupling has been put to overcritical, with the target to have a loaded quality factor about 4 times smaller than the axion line-width. This is important for what concern data analysis. Data taking is divided in different units that we usually call RUN, each RUN differing from another normally for the cavity central frequency that can be varied with the sapphire triplets described above. The detection chain system noise temperature and gain have been measured once at the beginning of the scanning session, and we monitored the stability of the gain with time by injecting a rf pure tone of amplitude -90 dBm on line L3 using SG2 at a frequency 900 kHz above the LO frequency. The LO frequency is chosen in order to keep the cavity frequency in a central band of the ADC working region. Each data taking step is composed of the following actions:

**action 1:** Set the cavity frequency to the desired value by moving the sapphire triplets. Set the LO frequency: this is actually not done for every step, since normally the change in cavity frequency is much smaller of the ADC bandwidth.

**action 2:** Measure a cavity reflection spectrum by tracking generator SG2 with the spectrum analyser SA.

Data are saved on a file to be fitted to deduce the antenna coupling  $\beta$

**action 3:** Measure a cavity transmission spectrum by using the noise source on line L1 and acquiring data with the ADC. Data are also taken with the the spectrum analyser SA for quick analysis. The number of 4 s blocks acquired with the ADC is normally about 30.

**action 4:** Measure the cavity output with all the inputs off, acquiring data with the ADC. This is the axion search data, and normally we collect 500 blocks of 4 s length each. Some RUNs have been done with a larger number of blocks. Again, data are also taken with the the spectrum analyser SA for quick analysis.

Table III summarizes all the scans performed. Figure 5 shows all the vacuum spectra measured with the spectrum analyser. Such plots are only taken for control purpose, while the data sampled by the ADC and stored in the computer are those used for the search and will be discussed in Section III.

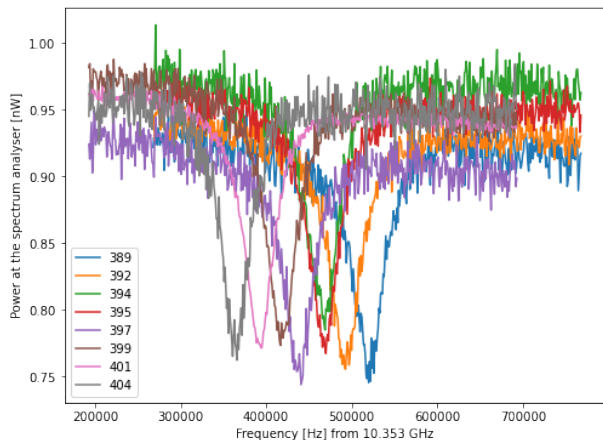


FIG. 5. Cumulative plots of the vacuum measurements with the magnet energized. Such plots are taken using the spectrum analyser, i.e. at the point P4 of Figure 2, only for control purpose during data taking and are not used in the data analysis. The different levels outside the resonance is a measure of the gain stability of the system: kept within a few percent in a 17 hours time span. RBW = 1000 Hz. INSERTARE UNITA NEL DISEGNO E NOME DELLE TRACCE. CERCARE VALORE DI RBW PER QUESTE FIGURE

## 6. Raw data processing

The 4 s long time sequences produced by the ADC are divided into chunks about 1.5 ms long, which are Fourier transformed and averaged. Another averaging is then performed to obtain a single power spectrum  $PS_n$

for each RUN having a resolution of 651 Hz and covering the down converted window  $[-1, +1]$  MHz. A raw data processing is performed to obtain relevant parameters. This is the same procedure already described in [29]. In particular, the antenna coupling  $\beta$  is obtained by fitting the cavity reflection spectrum measured with the spectrum analyser SA with tracking generator SG2 (see 'action 2'). The cavity loaded quality factor  $Q_L$  and central frequency  $\nu_c$  are obtained by fitting the average spectra obtained from the ADC data collected while the diode noise source was at the input of line L1 (see 'action 3'). The resulting parameters are reported in Table IV. The table reports also the amplitude of the reference peak set to the frequency +900 kHz in the down converted spectra. This measurement shows again that the stability of the detection chain gain was within a few percent along the complete data taking.

RUN n	$\nu_c - 10.353$ GHz (Hz)	Cavity $Q_L$	$\beta$	Ref Peak (a.u.)
389	522 551	230 000	10.86	179
392	494 103	240 000	11.98	185
394	468 841	245 000	12.17	186
395	468 841	245 000	12.17	187
397	439 835	245 000	11.43	175
399	418 536	245 000	11.43	191
401	393 135	250 000	11.37	186
404	365 376	255 000	11.86	193

TABLE IV. Summary of the parameters obtained by the fits of preliminary data for all the RUNs performed. Ref Peak is the amplitude of the reference peak due to the pure tone injected by SG2 on line L3 during data taking at a frequency 900 kHz above the reference oscillator of the mixer.

During the raw analysis, a careful check of the ADC data compared with the SA data has evidenced a problem present in the down-converted data. The ADC input is filtered by a single pole low pass filter having the -3 dB point at about 1.7 MHz. Unfortunately this is not enough to avoid aliasing of the rather flat noise input. From the comparison of the high frequency and down converted spectra we estimate that the added noise is about a factor 1.7 of the average noise in the vicinity of the cavity resonance.

Each power spectrum  $PS_n$  is the readout of the ADC input, and to obtain the power at the cavity output it must be divided by the overall gain. Alternatively, one equals the noise level measured at the ADC with the power given by the effective noise temperature of the system. We have assumed that the system noise temperature has not changed over the entire data taking time, having a duration of 17 hours. Indeed, the relative error of the  $T_{sys}$ , about 6.3 %, is larger of the relative changes of the reference peak as obtained by Table IV having a maximum of 5.1 %. For each RUN we assume that the noise level at the cavity frequency is

$$P_n(\nu) = k_B T_{sys}^{ADC} B \quad (6)$$

where  $B = 651$  Hz is the bin width,  $k_B$  is the Boltzmann's constant, and  $T_{\text{sys}}^{\text{ADC}} = 1.7 T_{\text{sys}} = 3.5$  K.

### III. DATA ANALYSIS AND RESULTS

#### A. Axion Detection procedure

Detection algorithms can be discussed in the classical "hypothesis testing" framework: on the basis of the observed data, we must decide whether to reject or fail to reject the null hypothesis (data are consistent with noise) against the alternative hypothesis (noise and signal are present in data) usually by means of a detection threshold determined by the desired significance level. At this stage of analysis, a signal due to genuine axion-photon coupling is indistinguishable from unmodelled noise sources due to the similar stochastic properties of noise and expected signal. The outcome of this data analysis step is a set of "axion candidate" masses or frequencies. However, axion signal has some distinctive properties that can be used to discriminate it from spurious detected signals (see Sect. III.B). We emphasize that the basis of our detection algorithm is a very robust model of the noise that allow us to use maximum likelihood criterion (i.e. a  $\chi^2$  test) to implement the decision rule. Deviations from the model of the noise power spectral density are clues of excess power that could be associated to a signal. In the frequency domain, the noise model for the power spectral density at the haloscope output (under the general assumptions of linearity, stationarity, ergodicity and single-resonance system) is simply a first order polynomial ratio

$$P(\nu) = \frac{\Delta_p + i\nu_p}{\Delta_z + i\nu_z} \quad (7)$$

where  $\Delta_p + i\nu_p$  and  $\Delta_z + i\nu_z$  are the pole and the zero values in the complex plane, respectively, where the  $\Delta$  are frequency differences. The fitting function to the power spectrum data, with fit parameters  $a, b, \dots, f$ , reads

$$F(\nu) = e^2 * \frac{|\nu - a + ib|^2}{|\nu - c + id|^2} + f * (\nu - c) \quad (8)$$

where the linear term accounts for the slight dependence of the ADC gain on frequency and we made the approximation  $\nu^2 - \nu_{p,z}^2 \simeq 2\nu_{p,z}(\nu - \nu_{p,z})$ . The parameters  $e$  is a normalization factor. The estimate of power spectrum resides on the Bartlett method of averaging periodograms. For every measured RUN of table III we performed the fit with  $F(\nu)$  and used the  $\chi^2$  to test the hypothesis of no signal. We discovered that the quality, i.e. the value for example of the reduced  $\chi^2$ , of the fits was worsening with the duration of the RUN. Indeed, a key issue is the stability of our set-up, where it is actually not surprisingly that drifts will appear over time scales of several ours. For this reason we decided, for the analysis procedure, to split every RUN in subruns with a fixed length of 2000 s, and to perform the fits on each of the resulting 23 subruns. For each subrun, the fits is performed on a window

of 200 bins (bin width = 651 Hz) centered at the cavity peak frequency. The weight on each bin is the measured value divided by  $\sqrt{N}$ ,  $N$  is the number of averages: for a 2000 s duration and 651 Hz bin width,  $N \simeq 1.37 \cdot 10^6$ . The null hypothesis  $H_0$  is accepted for  $\chi^2$  probability above the chosen threshold of  $P_\alpha = 0.001$ . Since for all subruns  $H_0$  was accepted, it is then possible to build a grand spectrum of all the residuals of the different fits, which will result in an increased sensitivity. The grand spectrum is built by a vertical weighted average of all the residual, again using as weight the values previously used to do the fits. Vertical average means that are performed at each bin value. The grand spectrum of the residuals and the relative histograms of the normalized values are shown in figure 6. The grand spectrum has 442 bins, a total  $\chi^2 = 452$  having a probability  $P = 0.37$ , which allowed us to accept the hypothesis of data compatible with pure thermal noise. Such a claim is done without modeling the axion, but imaging it is spread all over the detection bandwidth. The minimum value of the  $\sigma$  of the residuals in Figure 6 is  $(6.2 \pm 0.4) \cdot 10^{-24}$  W, obtained at the frequency of 403645 Hz shifted from 10.353 GHz with a total integration time of 36000 s. The value expected from Dicke's radiometer equation is  $(6.5 \pm 0.4) \cdot 10^{-24}$  W.

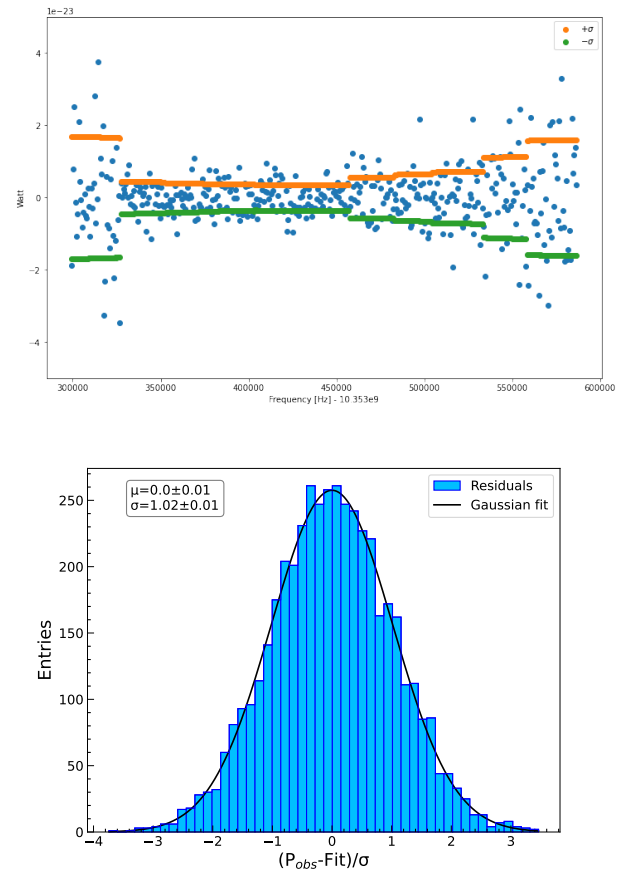


FIG. 6. Grand spectrum of the residuals. (a) Residuals and their sigma versus frequency. The bin size is 651 Hz. (b) Histogram of the normalized residuals

## B. Axion Discrimination procedures

Candidates that survive to a simple repetition of the  $\chi^2$  test (using a new data set taken in the same experimental conditions) can be further discriminated using a stationarity and on-off resonance tests. A stationarity test verifies that a signal is continuously present during a data taking. An on-off resonance test verifies that the signal can be maximized by a tuning procedure of the cavity. Moreover, the dependence of signal power on the antenna coupling  $\beta$  can also be checked. Eventually, a change of the magnetic field allow us to verify if the signal power is proportional to the magnetic field squared. Candidates that passed this step would be associated to axionic dark matter. When no axion candidate survive at the sensitivity level of KSVZ or DFSZ models, an upper limit on axion-photon coupling can be set for the standard model of Galaxy halo. However, such sensitivity requirements do not hold for upper limits on Axion Like Particles (ALPs) couplings.

## C. Upper limits on axion-photon coupling

Having data compatible with the presence of only noise, we can then proceed to derive bounds on the coupling constant of the axion to the photon, assuming specific coupling and galactic halo models. Bounds can be inferred by evaluating the detection efficiency via Monte Carlo techniques.

The detection efficiency, which is the information complementing noise estimation, can be evaluated via Monte Carlo techniques when we assume a specific model for axion signal, for instance the standard reference model in the axion literature [..]. After an assessment of detection efficiency, an upper limit at the desired confidence level, readily follows. In this standard framework, the expected power spectrum generated by the axion conversion inside the haloscope, when the haloscope bandwidth is greater than the axion bandwidth, is given by [39, 48]:

$$P_a = \left( \frac{g_{a\gamma\gamma}^2}{m_a^2} \hbar^3 c^3 \rho_a \right) \left( \frac{\beta}{1+\beta} \omega_c \frac{1}{\mu_0} B_0^2 V C_{030} Q_L \right) \times \left( \frac{1}{1 + (2Q_L \Delta\omega/\omega_c)^2} \right) \quad (9)$$

In the first set of parenthesis,  $\rho_a \sim 0.45 \text{ GeV/cm}^3$  [49] is the local dark matter density,  $g_{a\gamma\gamma}$  is the coupling constant of the axion-photon interaction,  $m_a$  is the axion mass. The second set of parenthesis contains the vacuum permeability  $\mu_0$ , the magnetic field  $B_0$  and the volume  $V$  of the cavity.  $\omega_c = 2\pi\nu_c$  is the resonance angular frequency of the cavity,  $\beta$  and  $Q_L$  are antenna coupling and loaded quality factor as described above.  $C_{030}$  is a geometrical factor equal to about 0.028 for the TM030 mode of this cylindrical dielectric cavity. In the third brackets, a Lorentzian function describes the effect of the detuning

$\Delta_w = \omega_c - \omega_a$  between the cavity and an axion having angular frequency  $\omega_a$ . In presence of a signal due to axion-photon conversion, an excess power would be observable in the residuals of the power spectrum fit to the noise model.

In the laboratory frame, the axion signal is expected to have a width of about 10 kHz [6, 50]. With a power spectrum with bin width  $\Delta\nu = 651 \text{ Hz}$  we expect the axion signal to be distributed over 16 consecutive bins.

## IV. RESULTS

$\sigma_{\text{Dicke}}$  calculated with the Dicke radiometer equation [51]

$$\sigma_{\text{Dicke}} = k_B T_{\text{sys}} \sqrt{\Delta\nu/\Delta t}, \quad (10)$$

where  $T_{\text{sys}}$ , is the system noise-temperature,  $\Delta\nu$  is the bin width (651 Hz) and  $\Delta t$  is the integration time (3000 s).

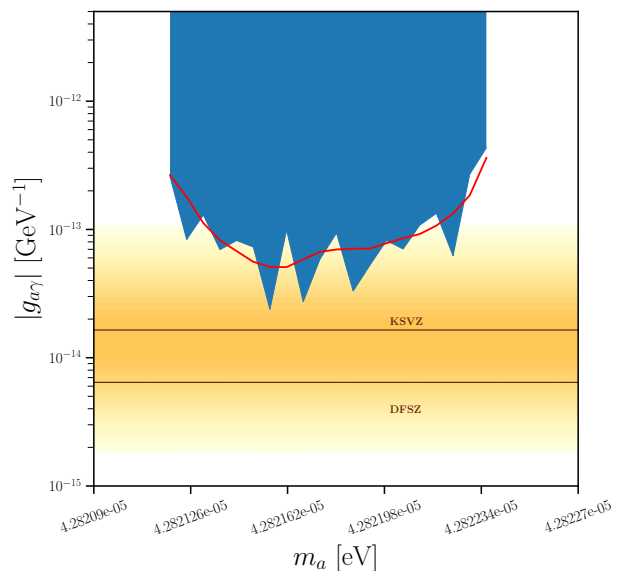


FIG. 7. insirire didascalica

## V. CONCLUSIONS

We reported the results of the search of galactic axions using an high-Q dielectric haloscope instrumented with a detection chain working close to the fundamental limit. The investigated mass range is  $42.xx - 42.yy \text{ } \mu\text{eV}$ , partially already investigated by us in a previous run and partially not currently accessible by other experiments.

## ACKNOWLEDGMENTS

We are grateful to E. Berto, A. Benato, and M. Rebeschini for the mechanical work; F. Calao and M. Tes-



saro for help with the electronics and cryogenics. We thank G. Galet and L. Castellani for the development of the magnet power supply, and M. Zago who realized the technical drawings of the system. We deeply acknowledge the Cryogenic Service of the Laboratori Nazionali di Legnaro for providing us with large quantities of liquid helium on demand. This work was supported by INFN and partially supported by EU through FET Open SU-

PERGALAX project, Grant N.863313.  
TO BE COMPLETED

### Appendix: Details on the experimental set up

Table V shows the relevant components used in the experimental set-up

- 
- [1] S. Weinberg, A new light boson?, *Phys. Rev. Lett.* **40**, 223 (1978).
  - [2] F. Wilczek, Problem of strong p and t invariance in the presence of instantons, *Phys. Rev. Lett.* **40**, 279 (1978).
  - [3] R. D. Peccei and H. R. Quinn, Cp conservation in the presence of pseudoparticles, *Phys. Rev. Lett.* **38**, 1440 (1977).
  - [4] J. Preskill, M. B. Wise, and F. Wilczek, Cosmology of the invisible axion, *Phys. Lett. B* **120**, 127 (1983).
  - [5] I. G. Irastorza and J. Redondo, New experimental approaches in the search for axion-like particles, *Prog. Part. Nucl. Phys.* **102**, 89 (2018).
  - [6] P. Sikivie, Experimental tests of the “invisible” axion, *Phys. Rev. Lett.* **51**, 1415 (1983).
  - [7] P. Sikivie, Detection rates for “invisible”-axion searches, *Phys. Rev. D* **32**, 2988 (1985).
  - [8] T. Braine, R. Cervantes, N. Crisosto, N. Du, S. Kimes, L. Rosenberg, G. Rybka, J. Yang, D. Bowring, A. Chou, *et al.*, Extended search for the invisible axion with the axion dark matter experiment, *Phys. Rev. Lett.* **124**, 101303 (2020).
  - [9] N. Du, N. Force, R. Khatiwada, E. Lentz, R. Ottens, L. Rosenberg, G. Rybka, G. Carosi, N. Woollett, D. Bowring, *et al.*, Search for invisible axion dark matter with the axion dark matter experiment, *Phys. Rev. Lett.* **120**, 151301 (2018).
  - [10] C. Boutan, M. Jones, B. H. LaRoque, N. Oblath, R. Cervantes, N. Du, N. Force, S. Kimes, R. Ottens, L. Rosenberg, *et al.*, Piezoelectrically tuned multimode cavity search for axion dark matter, *Phys. Rev. Lett.* **121**, 261302 (2018).
  - [11] C. Bartram *et al.*, *Phys. Rev. Lett.* **127**, 261803 (2021).
  - [12] K. M. Backes, D. A. Palken, S. A. Kenany, B. M. Brubaker, S. Cahn, A. Droster, G. C. Hilton, S. Ghosh, H. Jackson, S. K. Lamoreaux, *et al.*, A quantum enhanced search for dark matter axions, *Nature* **590**, 238 (2021).
  - [13] L. Zhong, S. Al Kenany, K. Backes, B. Brubaker, S. Cahn, G. Carosi, Y. Gurevich, W. Kindel, S. Lamoreaux, K. Lehnert, *et al.*, Results from phase 1 of the haystac microwave cavity axion experiment, *Phys. Rev. D* **97**, 092001 (2018).
  - [14] B. T. McAllister, G. Flower, E. N. Ivanov, M. Goryachev, J. Bourhill, and M. E. Tobar, The organ experiment: An axion haloscope above 15 ghz, *Phys. Dark Univ.* **18**, 67 (2017).
  - [15] A. Quiskamp, B. T. McAllister, P. Altin, E. N. Ivanov, M. Goryachev, and M. E. Tobar, Direct search for dark matter axions excluding alpogenesis in the 63- to 67-&#x3bc;ev range with the organ experiment, *Science Advances* **8**, eabq3765 (2022).
  - [16] J. Choi, S. Ahn, B. Ko, S. Lee, and Y. K. Semertzidis, Capp-8tb: Axion dark matter search experiment around 6.7  $\mu\text{eV}$ , *Nucl. Inst. Meth. Phys. Res. A* **1013**, 165667 (2021).
  - [17] S. Lee, S. Ahn, J. Choi, B. Ko, and Y. K. Semertzidis, Axion dark matter search around 6.7  $\mu\text{eV}$ , *Phys. Rev. Lett.* **124**, 101802 (2020).
  - [18] J. Jeong, S. Youn, S. Bae, J. Kim, T. Seong, J. E. Kim, and Y. K. Semertzidis, Search for invisible axion dark matter with a multiple-cell haloscope, *Phys. Rev. Lett.* **125**, 221302 (2020).
  - [19] O. Kwon, D. Lee, W. Chung, D. Ahn, H. Byun, F. Caspers, H. Choi, J. Choi, Y. Chong, H. Jeong, *et al.*, First results from an axion haloscope at capp around 10.7  $\mu\text{eV}$ , *Phys. Rev. Lett.* **126**, 191802 (2021).
  - [20] Y. Lee, B. Yang, H. Yoon, M. Ahn, H. Park, B. Min, D. Kim, and J. Yoo, Searching for invisible axion dark matter with an 18 t magnet haloscope, *Phys. Rev. Lett.* **128**, 241805 (2022).
  - [21] C. M. Adair, K. Altenmüller, V. Anastassopoulos, S. A. Cuendis, J. Baier, K. Barth, A. Belov, D. Bozicevic, H. Bräuninger, G. Cantatore, F. Caspers, J. F. Castel, S. A. Çetin, W. Chung, H. Choi, J. Choi, T. Dafni, M. Davenport, A. Dermenev, K. Desch, B. Döbrich, H. Fischer, W. Funk, J. Galan, A. Gardikiotis, S. Gninenko, J. Golm, M. D. Hasinoff, D. H. H. Hoffmann, D. D. Ibáñez, I. G. Irastorza, K. Jakovčić, J. Kaminski, M. Karuza, C. Krieger, Ç. Kutlu, B. Lakić, J. M. Laurent, J. Lee, S. Lee, G. Luzón, C. Malbrunot, C. Margalejo, M. Maroudas, L. Miceli, H. Mirallas, L. Obis, A. Özbey, K. Özbozdoğan, M. J. Pivovarov, M. Rosu, J. Ruz, E. Ruiz-Chóliz, S. Schmidt, M. Schumann, Y. K. Semertzidis, S. K. Solanki, L. Stewart, I. Tsagris, T. Vafeiadis, J. K. Vogel, M. Vretenar, S. Youn, and K. Zioutas, Search for dark matter axions with CAST-CAPP, *Nature Communications* **13**, 10.1038/s41467-022-33913-6 (2022).
  - [22] T. Grenet, R. Ballou, Q. Basto, K. Martineau, P. Perrier, P. Pugnât, J. Quevillon, N. Roch, and C. Smith, *arXiv:2110.14406* (2021).
  - [23] A. Á. Melcón, S. A. Cuendis, C. Cogollos, A. Díaz-Morcillo, B. Döbrich, J. D. Gallego, J. Barceló, B. Gimeno, J. Golm, I. G. Irastorza, *et al.*, Scalable haloscopes for axion dark matter detection in the 30  $\mu\text{eV}$  range with rades, *JHEP* **07** (2020), 084.
  - [24] A. A. Melcon, S. A. Cuendis, C. Cogollos, A. Díaz-Morcillo, B. Döbrich, J. D. Gallego, B. Gimeno, I. G. Irastorza, A. J. Lozano-Guerrero, C. Malbrunot, *et al.*, Axion searches with microwave filters: the rades project, *JCAP* **05** (2018), 040.

Components	Type	Model	Parameters @ 10 GHz
Cryogenic set up - Figure 1			
K1, K2, K3	Attenuators	Hewlett Packard 8493B 20 DB	IL = 20 dB
C1	Circulator	Raditek RADC-8-12-Cryo-0.02-4K-S23-1WR-MS-b	IL = 0.6 dB
C2, C3	Isolator	Raditek RAD1-8-12-Cryo-0.02-4K-S23-1WR-MS-b	IL = 0.6 dB
HP	High Pass Filter	Mini Circuit VHF-7150+	IL = 0.7 dB
Cables	RF Cable	KeyCom ULT-05	IL = 1.9 dB/m
Cables	SC RF Cable	KeyCom NbTiNbTi085	–
HEMT	Amplifier	Low Noise Factory LNF-LNC4-16B	Gain = 42 dB
①	Thermometer	ICE Oxford RuO2 RCWPM 1206-68-2.21 KOHM	
$I_{DC}$	Current source	Keithley 263	
Room temperature set up - Figure 2			
K4	Attenuator	Narda Micro-Pad 4779 - 12	IL = 12 dB
Cables	RF Cable	Huber - Suhner SF104	IL = 1 dB/m
CD1	Power Splitter	Macom 1147	
CD2	Power Combiner	Triangle Microwave YL - 74	
HEMT	Amplifier	Low Noise Factory LNF-LNR4-16B	Gain = 35 dB
AI, AQ	Amplifier	Femto DPHVA-101	Gain (1 MHz) = 50 dB
Mixer	Mixer	Miteq IRM0812LC2Q	–
A1	Amplifier	MITEQ AFS4-08001200-10-CR-4	Gain = 32 dB
Noise Source	Noise Source	Micronetics NS346B	$T_{eff} = 10000$ K
SG1, SG2, LO, PUMP	Signal Generator	Keysight N5183/N5173	
SA	Spectrum Analyser	Keysight N9010B	
ADC	Analog to digital Converter	National Instruments USB 6366	Rate = 2 Ms/s

TABLE V. Description of the relevant components for the experimental setup. IL = Insertion Loss.

- [25] A. Álvarez Melcón, S. Argüedas Cuendis, J. Baier, K. Barth, H. Bräuninger, S. Calatroni, G. Cantatore, F. Caspers, J. Castel, S. A. Cetin, *et al.*, First results of the cast-rades haloscope search for axions at  $34.67 \mu\text{eV}$ , *JHEP* **10** (2021), 075.
- [26] H. Chang, J.-Y. Chang, Y.-C. Chang, Y.-H. Chang, Y.-H. Chang, C.-H. Chen, C.-F. Chen, K.-Y. Chen, Y.-F. Chen, W.-Y. Chiang, W.-C. Chien, H. T. Doan, W.-C. Hung, W. Kuo, S.-B. Lai, H.-W. Liu, M.-W. OuYang, P.-I. Wu, and S.-S. Yu (TASEH Collaboration), Taiwan axion search experiment with haloscope: Cd102 analysis details, *Phys. Rev. D* **106**, 052002 (2022).
- [27] D. Alesini, C. Braggio, G. Carugno, N. Crescini, D. D’Agostino, D. Di Gioacchino, R. Di Vora, P. Falferi, S. Gallo, U. Gambardella, *et al.*, Galactic axions search with a superconducting resonant cavity, *Phys. Rev. D* **99**, 101101 (2019).
- [28] D. Alesini, C. Braggio, G. Carugno, N. Crescini, D. D’Agostino, D. Di Gioacchino, R. Di Vora, P. Falferi, U. Gambardella, C. Gatti, *et al.*, Search for invisible axion dark matter of mass  $m_a = 43 \mu\text{eV}$  with the quax- $\alpha$   $\gamma$  experiment, *Phys. Rev. D* **103**, 102004 (2021).
- [29] D. Alesini, D. Babusci, C. Braggio, G. Carugno, N. Crescini, D. D’Agostino, A. D’Elia, D. Di Gioacchino, R. Di Vora, P. Falferi, U. Gambardella, C. Gatti, G. Iannone, C. Ligi, A. Lombardi, G. Maccarrone, A. Ortolan, R. Pengo, A. Rettaroli, G. Ruoso, L. Taffarello, and S. Tocci, Search for galactic axions with a high- $q$  dielectric cavity, *Phys. Rev. D* **106**, 052007 (2022).
- [30] R. Barbieri, C. Braggio, G. Carugno, C. S. Gallo, A. Lombardi, A. Ortolan, R. Pengo, G. Ruoso, and C. C. Speake, Searching for galactic axions through magnetized media: the quax proposal, *Phys. Dark Univ.* **15**, 135 (2017).
- [31] N. Crescini, D. Alesini, C. Braggio, G. Carugno, D. Di Gioacchino, C. Gallo, U. Gambardella, C. Gatti, G. Iannone, G. Lamanna, *et al.*, Operation of a ferromagnetic axion haloscope at  $m_a = 58 \mu\text{eV}$ , *Eur. Phys. J. C* **78**, 1 (2018).
- [32] N. Crescini, D. Alesini, C. Braggio, G. Carugno, D. D’Agostino, D. Di Gioacchino, P. Falferi, U. Gambardella, C. Gatti, G. Iannone, *et al.*, Axion search with a quantum-limited ferromagnetic haloscope, *Phys. Rev. Lett.* **124**, 171801 (2020).
- [33] C. Gatti, D. Alesini, D. Babusci, C. Braggio, G. Carugno, N. Crescini, D. Di Gioacchino, P. Falferi, G. Lamanna, C. Ligi, *et al.*, The klash proposal: Status and perspectives, [arXiv:1811.06754](https://arxiv.org/abs/1811.06754) (2018).
- [34] D. Alesini, D. Babusci, F. Björkeröth, F. Bossi, P. Ciambone, G. D. Monache, D. Di Gioacchino, P. Falferi, A. Gallo, C. Gatti, *et al.*, Klash conceptual design report, [arXiv:1911.02427](https://arxiv.org/abs/1911.02427) (2019).
- [35] A. Caldwell, G. Dvali, B. Majorovits, A. Millar, G. Raffelt, J. Redondo, O. Reimann, F. Simon, F. Steffen, M. W. Group, *et al.*, Dielectric haloscopes: a new way to detect axion dark matter, *Phys. Rev. Lett.* **118**, 091801 (2017).
- [36] T. M. collaboration, S. Knirck, J. Schütte-Engel, S. Beurthey, D. Breitmoser, A. Caldwell, C. Diaconu, J. Diehl, J. Egge, M. Esposito, A. Gardikiotis, E. Garutti, S. Heyminck, F. Hubaut, J. Jochum, P. Karst, M. Kramer, C. Krieger, D. Labat, C. Lee, X. Li, A. Lindner, B. Majorovits, S. Martens, M. Matysek, E. Öz, L. Planat, P. Pralavorio, G. Raffelt, A. Ranadive, J. Redondo, O. Reimann, A. Ringwald, N. Roch, J. Schaffran, A. Schmidt, L. Shtembari, F. Steffen, C. Strandhagen, D. Strom, I. Usherov, and G. Wieching, Simulating madmax in 3d: requirements for dielectric

- axion haloscopes, *Journal of Cosmology and Astroparticle Physics* **2021** (10), 034.
- [37] M. Lawson, A. J. Millar, M. Pancaldi, E. Vitagliano, and F. Wilczek, *Phys. Rev. Lett.* **123**, 141802 (2019).
- [38] A. J. Millar, S. M. Anlage, R. Balafendiev, P. Belov, K. van Bibber, J. Conrad, M. Demarteau, A. Droster, K. Dunne, A. G. Rosso, J. E. Gudmundsson, H. Jackson, G. Kaur, T. Klaesson, N. Kowitt, M. Lawson, A. Leder, A. Miyazaki, S. Morampudi, H. V. Peiris, H. S. Røising, G. Singh, D. Sun, J. H. Thomas, F. Wilczek, S. Withington, and M. Wooten, *Alpha: Searching for dark matter with plasma haloscopes* (2022).
- [39] S. Al Kenany, M. Anil, K. Backes, B. Brubaker, S. Cahn, G. Carosi, Y. Gurevich, W. Kindel, S. Lamoreaux, K. Lehnert, *et al.*, Design and operational experience of a microwave cavity axion detector for the 20–100  $\mu\text{eV}$  range, *Nucl. Instr. Meth. Phys. Res. A* **854**, 11 (2017).
- [40] D. Di Gioacchino, C. Gatti, D. Alesini, C. Ligi, S. Tocci, A. Rettaroli, G. Carugno, N. Crescini, G. Ruoso, C. Braggio, *et al.*, Microwave losses in a dc magnetic field in superconducting cavities for axion studies, *IEEE Trans. App. Sup.* **29**, 1 (2019).
- [41] D. Ahn, O. Kwon, W. Chung, W. Jang, D. Lee, J. Lee, S. W. Youn, D. Youm, and Y. K. Semertzidis, Maintaining high q-factor of superconducting  $\text{YBa}_2\text{Cu}_3\text{O}_{7-x}$  microwave cavity in a high magnetic field, [arXiv:1904.05111](https://arxiv.org/abs/1904.05111) (2019).
- [42] D. Alesini, C. Braggio, G. Carugno, N. Crescini, D. D’Agostino, D. Di Gioacchino, R. Di Vora, P. Falferi, U. Gambardella, C. Gatti, *et al.*, High quality factor photonic cavity for dark matter axion searches, *Rev. Sci. Instr.* **91**, 094701 (2020).
- [43] D. Alesini, C. Braggio, G. Carugno, N. Crescini, D. D’Agostino, D. Di Gioacchino, R. Di Vora, P. Falferi, U. Gambardella, C. Gatti, *et al.*, Realization of a high quality factor resonator with hollow dielectric cylinders for axion searches, *Nucl. Instr. Meth. Phys. Res. A* **985**, 164641 (2021).
- [44] R. Di Vora, D. Alesini, C. Braggio, G. Carugno, N. Crescini, D. D’Agostino, D. Di Gioacchino, P. Falferi, U. Gambardella, C. Gatti, G. Iannone, C. Ligi, A. Lombardi, G. Maccarrone, A. Ortolan, R. Pengo, A. Rettaroli, G. Ruoso, L. Taffarello, and S. Tocci, High- $q$  microwave dielectric resonator for axion dark-matter haloscopes, *Phys. Rev. Applied* **17**, 054013 (2022).
- [45] A. Ranadive, M. Esposito, L. Planat, E. Bonet, C. Naud, O. Buisson, W. Guichard, and N. Roch, Kerr reversal in josephson meta-material and traveling wave parametric amplification, *Nature Communications* **13**, 1737 (2022).
- [46] A. Marin, M. Bignotto, M. Bonaldi, M. Cerdonio, P. Falferi, R. Mezzena, G. A. Prodi, G. Soranzo, L. Taffarello, A. Vinante, S. Vitale, and J.-P. Zendri, Noise measurements and optimization of the high sensitivity capacitive transducer of AURIGA, *Classical and Quantum Gravity* **19**, 1991 (2002).
- [47] C. Braggio, G. Cappelli, G. Carugno, N. Crescini, R. Di Vora, M. Esposito, A. Ortolan, L. Planat, A. Ranadive, N. Roch, and G. Ruoso, A haloscope amplification chain based on a traveling wave parametric amplifier, *Review of Scientific Instruments* **93**, 094701 (2022).
- [48] B. M. Brubaker, L. Zhong, Y. V. Gurevich, S. B. Cahn, S. K. Lamoreaux, M. Simanovskaia, J. R. Root, S. M. Lewis, S. Al Kenany, K. M. Backes, I. Urdinaran, N. M. Rapidis, T. M. Shokair, K. A. van Bibber, D. A. Palken, M. Malnou, W. F. Kindel, M. A. Anil, K. W. Lehnert, and G. Carosi, First results from a microwave cavity axion search at 24  $\mu\text{eV}$ , *Phys. Rev. Lett.* **118**, 061302 (2017).
- [49] P. A. Zyla *et al.*, Review of Particle Physics, (Particle Data Group), *Prog. Theor. Exp. Phys.* **2020**, 10.1093/ptep/ptaa104 (2020), 083C01, <https://academic.oup.com/ptep/article-pdf/2020/8/083C01/34673722/ptaa104.pdf>.
- [50] M. S. Turner, Periodic signatures for the detection of cosmic axions, *Phys. Rev. D* **42**, 3572 (1990).
- [51] R. H. Dicke, The measurement of thermal radiation at microwave frequencies, in *Classics in Radio Astronomy* (Springer, Dordrecht, 1946) pp. 106–113.